iScience

CellPress
OPEN ACCESS

Article

Coking-resistant dry reforming of methane over Ni/γ-Al_2O_3 catalysts by rationally steering metal-support interaction

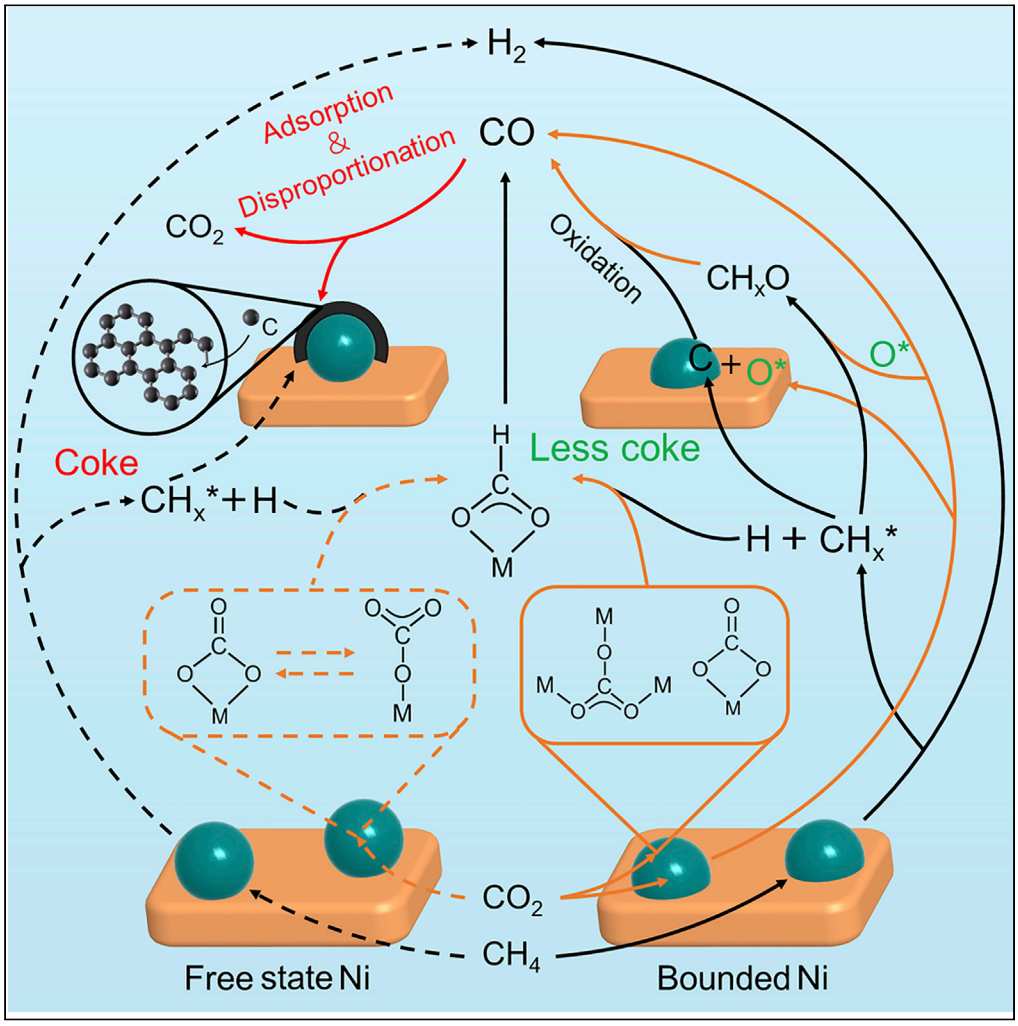

Bo Yang, Jiang Deng, Hongrui Li, Tingting Yan, Jianping Zhang, Dengsong Zhang

dszhang@shu.edu.cn

Highlights

The anti-coking ability of the bounded Ni is better than the free state Ni

The bounded Ni has a stronger ability to activate CO_2 to produce active O* species

High reactivity and stable polydentate carbonate enables efficient reaction

Rational metal-support interaction results in good resistance to CO poisoning

Yang et al., iScience 24, 102747
July 23, 2021
https://doi.org/10.1016/j.isci.2021.102747

iScience

CellPress
OPEN ACCESS

Article

Coking-resistant dry reforming of methane over Ni/γ-Al_2O_3 catalysts by rationally steering metal-support interaction

Bo Yang,[1,2] Jiang Deng,[1,2] Hongrui Li,[1] Tingting Yan,[1] Jianping Zhang,[1] and Dengsong Zhang[1,3,*]

SUMMARY

The coking issue is the main challenge for dry reforming of methane (DRM) over Ni-based catalysts. Herein, we excavate the reasons for the enhanced coking resistance of the bounded Ni over the free state Ni in Ni/γ-Al_2O_3 catalysts for DRM. Rational metal-support interaction of the bounded Ni would facilitate desorption of CO, thus suppressing CO disproportionation and decreasing carbon deposition. The higher activity of the bounded Ni is ascribed to better methane cracking ability, stronger adsorption, and activation of CO_2 by forming polydentate carbonate. The better activation of CO_2 over the bounded Ni would also contribute to the gasification of formed coke. We gain an insight into the anti-coking mechanism of DRM determined by metal-support interaction in Ni/γ-Al_2O_3 catalysts through mechanistic studies. It is believed that our findings would enlighten the design of more efficient catalysts for DRM.

INTRODUCTION

Dry reforming of methane (DRM) was attractive for industrial applications since it would simultaneously consume two kinds of greenhouse gases (CH_4 and CO_2) and produce the syngas (H_2 and CO) (Fletcher and Schaefer, 2019). The produced syngas with H_2/CO = 1 was conducive to downstream Fischer-Tropsch synthesis for high-value-added products. Noble metals were usually regarded as efficient reactive catalysts, but their inaccessibility and expensiveness would limit the practical use (Shi et al., 2013). As a replacement, the nickel-based catalyst was widely studied, thanks to its high activity and much cheaper price (Akri et al., 2019; Kim et al., 2017; Song et al., 2020). However, problems like sintering and coking of the catalysts have been hampering their commercial application (Li and Gong, 2014; Pakhare and Spivey, 2014; Zhang et al., 2021a).

γ-Al_2O_3 was extensively researched as support for nickel-based catalysts to catalyze DRM reaction because of its high surface area and good thermostability (Stroud et al., 2018). Actually, the reactivity of original Ni nanoparticles could be modulated by the oxide supports which would determine the DRM performance (Bu et al., 2019). For example, the acidic properties of γ-Al_2O_3 would contribute to the decomposition of CH_4, giving rise to good DRM activity (Osaki et al., 1995; Shehu et al., 2019). However, Al_2O_3-supported Ni catalysts still severely suffered from carbon accumulation due to the CH_4 decomposition and CO disproportionation (Dong et al., 2020; Joo et al., 2020). To enhance its ability of anti-coking, researchers tried to control the size of Ni particles via using specific precursors (Dama et al., 2018; Song et al., 2018) or increase the basicity of the support by incorporating alkali or alkaline earth metals into the support (Mette et al., 2016; Wang et al., 2013). Meanwhile, understanding the intrinsic activity and coke resistance behaviors of specific active sites in Ni/γ-Al_2O_3 was also very important for the design of better catalysts.

Ni would dissolve into γ-Al_2O_3 giving rise to nonstoichiometric spinel structure during calcination process, and partial Ni would exsolute from the spinel structure in the reduction process (Xu et al., 2001). Hence, three types of Ni, namely Ni^{2+} in spinel, the bounded Ni exsoluted from spinel, and the free state Ni on the surface of γ-Al_2O_3, possibly existed in the reduced Ni/γ-Al_2O_3 catalysts. These Ni species featured different metal-support interactions (MSIs), which would affect the performance of the catalyst in DRM. As proposed by some literatures, the tetra-coordinated Ni^{2+} in $NiAl_2O_4$ spinel structure was the active site for DRM (Rogers et al., 2016), and metallic Ni particles were less active but responsible for limited coking of the catalysts. However, some researchers concluded that metallic Ni on the surface rather than

[1]International Joint Laboratory of Catalytic Chemistry, Department of Chemistry, Research Center of Nano Science and Technology, College of Sciences, Shanghai University, 200444 Shanghai, China

[2]These authors contributed equally

[3]Lead contact

*Correspondence: dszhang@shu.edu.cn

https://doi.org/10.1016/j.isci.2021.102747

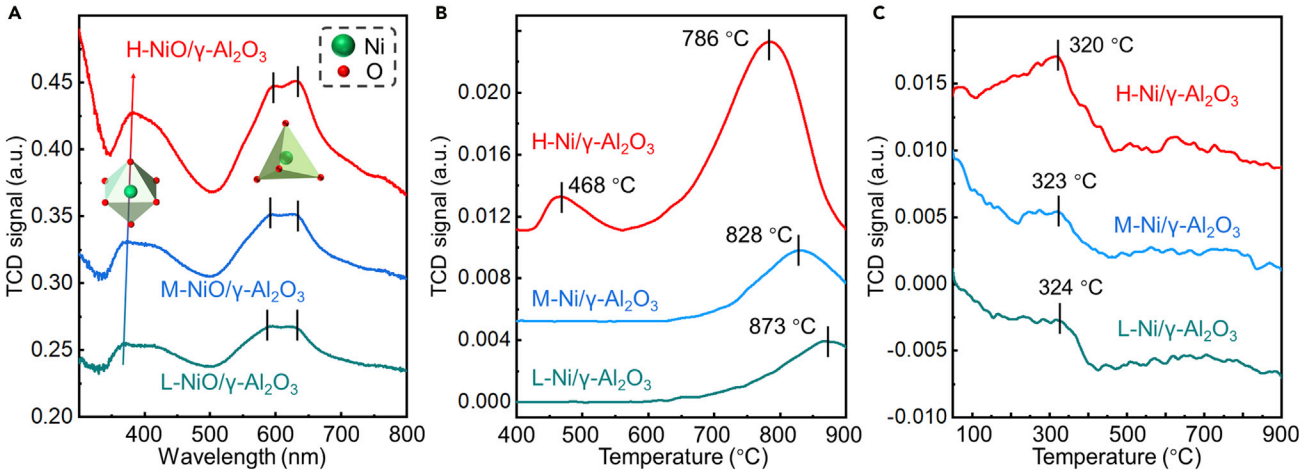

Figure 1. Structure characterization of the catalysts

(A) UV-vis spectra of the calcination samples.

(B) H_2-TPR profiles of serial catalysts.

(C) O_2-TPO profiles of the pre-reduced catalysts.

See also Figures S2–S9 and Tables S1, S2, and S5.

the Ni-Al_2O_3 interface was the active site in DRM, but the coke resistance behavior of specific active sites was still incompatible (Foppa et al., 2017). Normally, the Ni loading and experimental temperature (calcination (Zhou et al., 2015), reductions (Srifa et al., 2018), and reaction temperature (Cao et al., 2018)) would influence the properties of Ni which determined the DRM performance of Ni/γ-Al_2O_3. When the nickel aluminate (mass content of Ni $\geq$ 33.3 wt%) was directly used as the catalysts, their performance might be overstated (Rogers *et al.*, 2016) because CH_4 might firstly react with NiO to form Ni which would catalyze the DRM reaction subsequently. Additionally, it might be imperfect to explore the roles of different active sites without controlling the temperature or mass loading (Foppa *et al.*, 2017).

Herein, the types of active Ni were preciously tuned by controlling the Ni mass loading and the annealing temperature, and then, the primary reasons for the differences of DRM performance between the species were studied. The Ni content was 0.9 wt%, 1.5 wt%, and 5.0 wt%, and the corresponding calcination and the reduced samples were named as (L, M, and H)-NiO/γ-Al_2O_3 and (L, M, and H)-Ni/γ-Al_2O_3, respectively. Meanwhile, we also gave the reasons why we chose these metal loadings (Figure S1). Two types of active Ni sites (the bounded Ni in L-Ni/γ-Al_2O_3 and M-Ni/γ-Al_2O_3 and the free state Ni in H-Ni/γ-Al_2O_3) with different MSIs were identified in Ni/γ-Al_2O_3 via ultraviolet-visible spectroscopy (UV-vis), hydrogen temperature-programmed reduction (H_2-TPR), and oxygen temperature-programmed oxidation (O_2-TPO) tests. Activity tests and thermogravimetric analysis (TGA) proved that, compared to the free state Ni, the bounded Ni possessed better anti-coking ability (0.087 $g_c \cdot mmol_{Ni}^{-1} \cdot h^{-1}$ *vs* 0.167 $g_c \cdot mmol_{Ni}^{-1} \cdot h^{-1}$ for coking rate), higher intrinsic activity (11.2 s^{-1} *vs* 8.48 s^{-1} for CH_4 conversion and 13.7 s^{-1} *vs* 11.9 s^{-1} for CO_2 conversion), and more robust stability for DRM. According to the results of *in situ* diffuse reflectance infrared Fourier transform spectroscopy (*in situ* DRIFTS), the better anti-coking ability and higher turnover frequency (TOF) of the bounded Ni were ascribed to the superior CH_4 cracking capacity, stronger adsorption, and better activation of CO_2. Additionally, the bounded Ni showed weaker interaction with CO than that of the free state Ni, which contributed to desorption of the products and suppressed the CO disproportionation. Our work clarified the differences in the carbon resistance and reaction mechanism of the two active sites in the Ni/γ-Al_2O_3 catalyst induced by different MSIs. This mechanistic research was believed to pave a way for devising better catalysts for DRM by precisely controlling the type of active Ni species.

RESULTS

Structure of catalysts

UV-vis spectra of calcination samples are given in Figure 1A to illustrate the coordination state of nickel; all spectra were subtracted from the alumina background. It was clear that Ni^{2+} species occupying tetracoordinate sites appeared at 596 and 633 nm. These bands did not shift as Ni loading increased (Négrier et al.,

2005), which indicated that the coordination environment of Ni^{2+} at this site got no changes. However, the peak at 350 nm, which was attributed to the d-d transition of the octahedral Ni^{2+} (Margossian et al., 2017), shifted to 381 nm with Ni content increasing. The bathochromic shift could be associated with a weaker ligand field of Ni^{2+} (Margossian *et al.*, 2017). The intensity of the two characteristic peaks enhanced simultaneously with increased Ni loading, meaning that Ni occupied both tetracoordinate and hex-coordinated sites at the same time (Elias et al., 2019). For the reduced samples (Figure S2), the peak positions of UV-vis spectra were similar to each other. However, NiO species in H-Ni/γ-Al_2O_3 were observed at 233 and 346 nm possibly as a consequence of partial oxidation of surface Ni particles (Rahman et al., 2018) with weaker MSI.

X-ray diffraction (XRD) was then used to characterize the crystal structure of reduced catalysts (Figure S3). The peak appearing at 51.7° for H-Ni/γ-Al_2O_3 was indexed to the facet (111) of Ni (PDF#04–0850) (Zhang et al., 2017). The characteristic XRD peaks of Ni were negligible over both L-Ni/γ-Al_2O_3 and M-Ni/γ-Al_2O_3, which might attribute to the low mass loading and better dispersion. The results of Scanning Electron Microscope-Energy Dispersive Spectrometer (SEM-EDS) mapping of the catalysts also prove this point (Figure S4), where Ni species were well dispersed in L-Ni/γ-Al_2O_3 and M-Ni/γ-Al_2O_3, but obvious agglomeration of Ni species occurred for the H-Ni/γ-Al_2O_3. The grain size of Ni in H-Ni/γ-Al_2O_3 calculated by the Scherrer equation was about 11 nm, which also coincided with the results of transmission electron microscopy (TEM). As was seen in Figures S5–S7, the size of Ni particles slightly increased from 8.9 ± 1.3 for L-Ni/γ-Al_2O_3 to 11.3 ± 2.5 nm for H-Ni/γ-Al_2O_3. On the other hand, the specific surface area (SAA) (Figure S8 and Table S1) was similar with slight increase for the catalysts. The gradual increase of the SAA might be related to the decomposition of nitrate in the pores of the support during calcination process, where a large amount of gas was generated to expand the pores. The higher the metal loading, the more the SAA increased.

H_2-TPR was performed (Figure 1B) to investigate the MSI of the reduced catalysts. The peaks appeared above 750°C derived from Ni exsolution from nonstoichiometric $NiAl_xO_y$ spinel structure on the surface of Al_2O_3 support (Mette et al., 2016). The peak gradually shifted to lower temperatures with higher Ni loading, suggesting the weaker MSI (Margossian *et al.*, 2017). It was worth noting that the peak at 467°C only appeared in H-Ni/γ-Al_2O_3, which showed the existence of weak-bonded NiO species (Li et al., 2014). O_2-TPO of pre-reduced samples at 750°C was performed to further evaluate the catalysts' MSI and the oxidation resistance ability of active metals (Figure 1C). For H-Ni/γ-Al_2O_3, a strong peak appeared at 320°C which might be related to the oxidation of the weak-bonded Ni. By contrast, there was no obvious peak for L-Ni/γ-Al_2O_3 and M-Ni/γ-Al_2O_3 in the test temperature range. This might be attributed to their relatively strong MSI, which would make Ni species more difficult to be re-oxidized (Zhao et al., 2018). The results above showed that the relationship of MSI among the catalysts was L-Ni/γ-Al_2O_3>M-Ni/γ-Al_2O_3>H-Ni/γ-Al_2O_3.

The High Resolution-Transmission Electron Microscope (HR-TEM) images of the catalysts are shown in Figure S9 to determine the specific structure of the active sites in the catalysts. It could be observed that all the catalysts showed the (111) crystal plane of Ni with the lattice spacing of 0.204 nm (Bu et al., 2020), but the structures of the catalysts were still significantly different: a spinel overlayer was found on the Ni particle in L-Ni/γ-Al_2O_3 (Mette et al., 2016), while the distortion of Ni lattice without spinel layer was found for M-Ni/γ-Al_2O_3. For H-Ni/γ-Al_2O_3, the Ni particles exposed (111) crystal plane without obvious distortion and coated layer. The differences of HR-TEM images among these three catalysts suggested that the MSI would influence the properties of the Ni particles derived from exolution, then influencing the electronic state of Ni. This conclusion was further proved by X-ray photoelectron spectroscopy (Table S2) where higher binding energy was found in L-Ni/γ-Al_2O_3 and M-Ni/γ-Al_2O_3 compared with H-Ni/γ-Al_2O_3. Those results proved that two kinds of active Ni would emerge with increasing Ni loading: the Ni particles exsoluted from octahedral sites during reduction exhibited stronger MSI and were regarded as the bounded Ni. With high Ni content, another kind of Ni (the free state Ni) derived from weak-bonded NiO with weaker MSI would appear in H-Ni/γ-Al_2O_3.

Performance of catalysts

Deduced from the results of H_2-TPR and relevant tests (Figures S10–S14), the bounded Ni would gradually exsolute to replenish active sites for DRM during the reaction at high temperature (750°C) (Wong et al., 2019). It would make it difficult to distinguish the differences between the bounded Ni and the free state

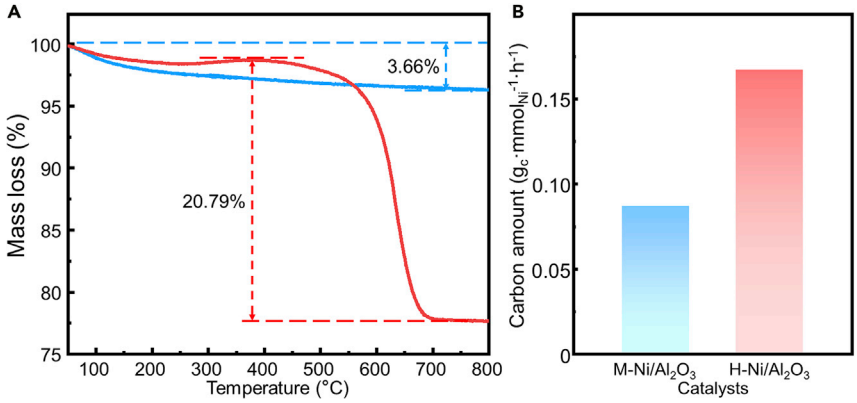

Figure 2. DRM performance of the catalysts

(A) TGA curves of the used M-(blue line) and H-Ni/γ-Al_2O_3 (red line) samples after 20-hr DRM test at 650°C.

(B) Coking rate of the spent samples after 20-hr DRM test at 650°C based on TGA results.

See also Figures S1 and S10–S20 and Tables S3, S4, and S6.

Ni. To accurately verify their differences of activity and coking resistance, a DRM test at lower temperature 650°C was adopted to exclude the effect of exsolution, with results listed in Figures 2 and S15–S19.

The results of the apparent reaction rate (CH_4) are shown in Figure S15. It was easy to observe that both L-Ni/γ-Al_2O_3 and M-Ni/γ-Al_2O_3 show similar reaction rates (530.6 $mmol \cdot min^{-1} \cdot g_{Ni}^{-1}$ and 565.3 $mmol \cdot min^{-1} \cdot g_{Ni}^{-1}$, respectively) derived from the bounded Ni. However, the initial reaction rate of H-Ni/γ-Al_2O_3 (131.5 $mmol \cdot min^{-1} \cdot g_{Ni}^{-1}$) was much lower compared to the former two samples. Combined with the previous analysis, it could be primarily inferred that the activity of the bounded Ni was higher than that of the free state Ni. Corresponding CO_2 apparent conversion rate (Figure S16) was higher than that of CH_4 because of the existence of reverse water gas shift reaction and Ni(111) possessed higher activation ability for CO_2 than CH_4 (Das et al., 2018; Foppa et al., 2016). It should also be noticed that M-Ni/γ-Al_2O_3 got less activity loss than L-Ni/γ-Al_2O_3 (52.4 $mmol \cdot min^{-1} \cdot g_{Ni}^{-1}$ to 181.2 $mmol \cdot min^{-1} \cdot g_{Ni}^{-1}$). This might be because when Ni loading was too low, the catalyst was more likely to be deactivated due to the dissolution of Ni into the support because of the too strong MSI during the reaction. Therefore, it could be speculated that a rational MSI was very important for the stability of the catalysts, as in the M-Ni/γ-Al_2O_3. The H_2/CO value of ~0.8 (Figure S17) was also similar with that of others (Al-Fatesh et al., 2020), and the mass balance and relationship between the actual reactant conversion and the thermodynamic equilibrium conversion were also given here. To further confirm the intrinsic activity between the two kinds of Ni, TOF for CH_4 and CO_2 was employed at 650°C (Figure S18 and Table S3). It was clear that M-Ni/γ-Al_2O_3 had higher TOF for both CH_4 and CO_2 than that of the H-Ni/γ-Al_2O_3 (11.2 s^{-1} *vs* 8.48 s^{-1} for CH_4, 13.7 s^{-1} *vs* 11.9 s^{-1} for CO_2), suggesting the higher intrinsic activity of the bounded Ni than the free state Ni. The TOF values of L-Ni/γ-Al_2O_3 were close to those of M-Ni/γ-Al_2O_3. It should also be noted that Ni/γ-Al_2O_3 with the bounded Ni was ahead of other catalysts in terms of the intrinsic activity (Table S4).

M-Ni/γ-Al_2O_3 and H-Ni/γ-Al_2O_3 were mainly used for the comparison in the next section while L-Ni/γ-Al_2O_3 would be omitted because L-Ni/γ-Al_2O_3 got similar active sites with M-Ni/γ-Al_2O_3 but was seriously deactivated in the reaction at 650°C. Severe carbon (21 wt%) accumulated on the H-Ni/γ-Al_2O_3 after 20 hr DRM test at 650°C, while the much lower coke (4 wt%) happened to M-Ni/γ-Al_2O_3 (Figure 2A). To eliminate the influence of active sites numbers on the amount of carbon deposit, the weight loss value was normalized to the active Ni, and the result is given in Figure 2B. The average coke amount of M-Ni/γ-Al_2O_3 was much lower than that of H-Ni/γ-Al_2O_3, which strongly verified that the bounded Ni had more excellent anti-carbon property than the free state Ni. SEM and TEM images of the used catalysts are given in Figure S19 to show morphology of catalysts after reaction. As described in the TGA results, the amount of carbon deposition observed in the used L-Ni/γ-Al_2O_3 and M-Ni/γ-Al_2O_3 samples was very small, while a large amount of coke species was observed in the used H-Ni/γ-Al_2O_3. With further observation, we found that these carbon deposition species should be mainly filamentous carbon and carbon nanotubes. On the other hand, XRD patterns of the used catalysts are listed in Figure S20 to study the reasons for catalysts' deactivation. It was easy to observe that a strong carbon species peak at 26° appeared in the XRD pattern of the spent H-Ni/γ-

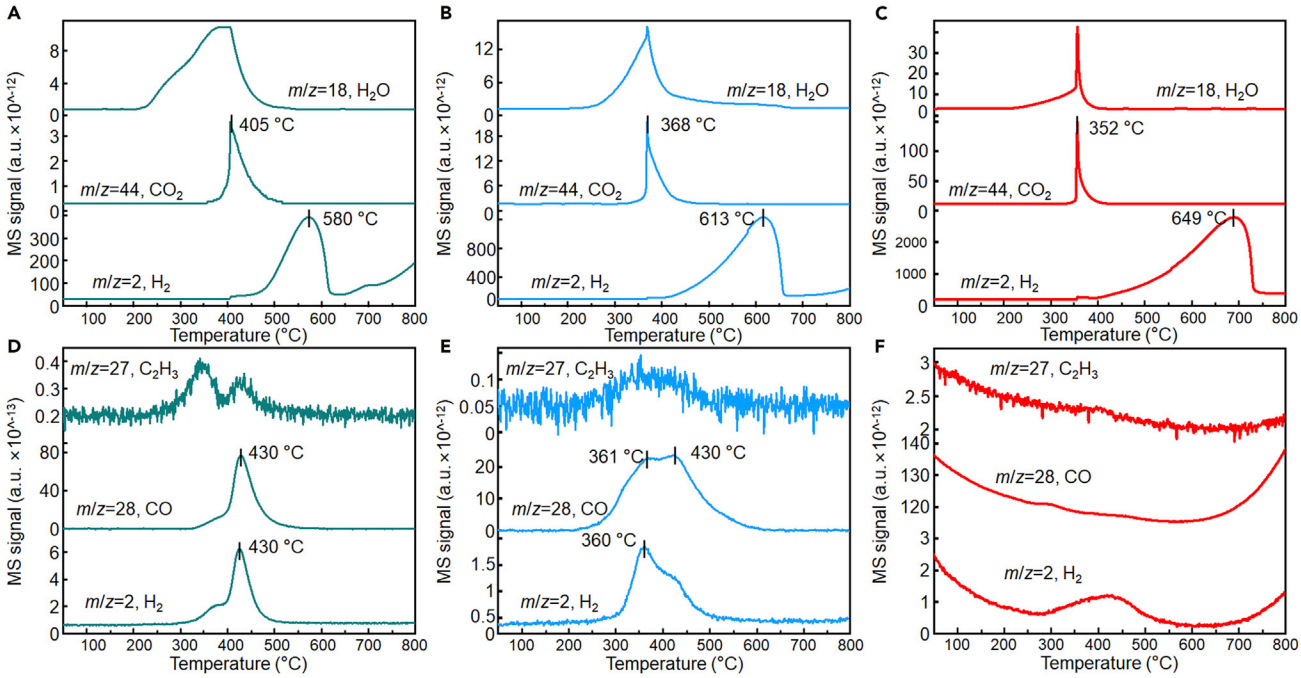

Figure 3. TPSR profiles of the catalysts

(A–C) (A) CH_4-TPSR MS profiles of L-Ni/γ-Al_2O_3, (B) M-Ni/γ-Al_2O_3, and (C) H-Ni/γ-Al_2O_3.

(D–F) (D) CH_4-CO_2 TPSR MS profiles of L-Ni/γ-Al_2O_3, (E) M-Ni/γ-Al_2O_3, and (F) H-Ni/γ-Al_2O_3.

See also Figure S21.

Al_2O_3. For used L-Ni/γ-Al_2O_3 and M-Ni/γ-Al_2O_3, the intensity of C species was very low, indicating that the amount of carbon deposition was small. At the same time, we found that after DRM reaction, Al_2O_3 was mainly in the γ phase, but α-Al_2O_3 (PDF#71–1123) was also observed at the diffraction angles of 35.04, 43.4, and 57.4, which correspond to (104), (113), and (116) crystal plane of α-Al_2O_3, respectively. This phenomenon showed that after a long-time test, the carrier Al_2O_3 underwent a partial transformation from γ phase to α phase. Nevertheless, the intrinsic activity, coking resistance, and stability of M-Ni/γ-Al_2O_3 were all better than those of H-Ni/γ-Al_2O_3, which might be related to the rational MSI of the bounded Ni in M-Ni/γ-Al_2O_3.

Temperature-programmed surface reaction mass spectra test

Summarizing from the previous characterization, the bounded and the free state Ni were proved to have different activity and anti-coking abilities for DRM. To explore the mechanism of these differences, a series of temperature-programmed surface reaction mass spectra (TPSR-MS) experiments were subsequently performed.

The results of CH_4 TPSR-MS are given in Figure 3A–3C. During the TPSR process, H_2 generation was always accompanied by CO_2 production which suggested CH_4 decomposed into H_2 and CH_x on the surface of Ni, while the latter would be oxidized on the surface of the catalysts to form CO and H_2. It should be noted that there was a signal mutation when H_2 starts to appear. This might be a consequence of a reaction between CH_4 and highly active O* species produced in the reduction process on the surface. The slope of the hydrogen generation signal decreased with the increase of Ni loading, which suggested that the bounded Ni presented better CH_4 activation ability. The signal of H_2 and CO_2 quickly decreased for all samples, possibly because of the limited amount of active O* on the surface of these catalysts. Subsequently, H_2 was secondarily generated deriving from the direct thermal cracking of CH_4 in the high temperature.

CH_4-CO_2 TPSR-MS experiment was performed to estimate the activation of CO_2, and the results are given in Figures 3D–3F. For L-Ni/γ-Al_2O_3 sample, peaks of CO appeared at 430°C. A similar peak was also noticed in M-Ni/γ-Al_2O_3 sample where a new low-temperature peak emerged at around 361°C, which

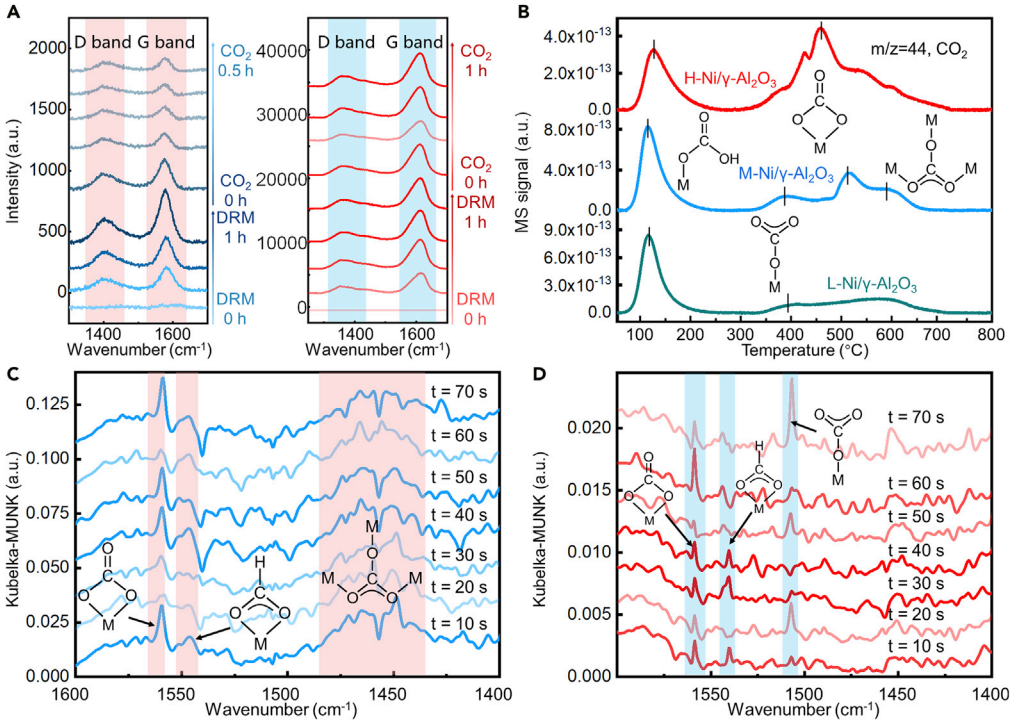

Figure 4. Reaction mechanism analysis

(A) Operando Raman spectra of the fresh samples (blue: M-Ni/γ-Al_2O_3, red: H-Ni/γ-Al_2O_3), test condition: 650°C, gas flow rate of CH_4 and CO_2: 15 mL/min, purge gas: 50 mL/min N_2.

(B) CO_2 signal in CO_2-TPD MS profiles of the catalysts.

(C) *In situ* DRIFTS of M-Ni/γ-Al_2O_3 at 650°C.

(D) *In situ* DRIFTS of H-Ni/γ-Al_2O_3 at 650°C.

See also Figures S22 and S23.

was due to more the bounded Ni of M-Ni/γ-Al_2O_3. In Figure 3F, nearly no signal of CO was detected in H-Ni/γ-Al_2O_3 between 200°C and 500°C, and the continuing release of CO happened above 600°C which suggested the weaker CO_2 activation ability and stronger interaction between CO and H-Ni/γ-Al_2O_3. This conclusion could be further proved by the results of CO-Temperature Programmed Desorption (CO-TPD) (Figure S21). The desorption temperature of CO from the surface of M-Ni/γ-Al_2O_3 was about 368°C, while for H-Ni/γ-Al_2O_3 it was 449°C. It could be inferred that the adsorption strength of CO on the free state Ni was stronger than that of the bounded Ni. It was also interesting to notice that H_2 production temperature was brought forward about 70°C compared to the counterparts in CH_4-TPSR, meaning that CO_2 activation could further favor H_2 production from CH_4 decomposition. Based on the results of TPSR-MS, the bounded Ni showed not only better capability toward CH_4 cracking than the free state Ni but also better activation ability for CO_2.

Operando Raman and *in situ* DRIFTS

Operando Raman tests were performed at 650°C to explain the differences in carbon deposition resistance of the M-Ni/γ-Al_2O_3 and H-Ni/γ-Al_2O_3 (Figure 4A). The DRM reaction was firstly carried out for around 1 hr until peak intensity of both D band (~1400 cm^{-1}) and G band (~1580 cm^{-1}) did not change significantly (Zhang et al., 2013); then, CH_4 was solely cut off to evaluate the effect of CO_2 on carbon species. For M-Ni/γ-Al_2O_3, carbon species accumulated gradually during the 1 hr DRM test. After cutting the CH_4 gas flow, the peak intensity at D and G band reduced immediately and eventually was steady for 15 min. On the contrary, the intensity of the G band peak of the H-Ni/γ-Al_2O_3 grew rapidly and remained stable for 10 min during the DRM test. After cutting CH_4, the intensity of the G band decreased at the 10th minute, but quickly rebounded at the 15th min, then keeping constant finally. The special rebound might be attributed to CO disproportionation to form carbon species since carbon deposition was more

likely to accumulate through CO disproportionation when MSI of Ni particles was not strong enough (Foppa *et al.*, 2016).

CO_2-Temperature Programmed Desorption Mass Spectrometer (CO_2-TPD MS) was carried out to explore the differences of CO_2 adsorption over the catalysts (Figure 4B). All samples got a sharp peak at about 90°C, which was attributed to desorption of weak-bonded bicarbonate (Keturakis et al., 2014). Smooth peaks at 370°C and 550°C, which originated from desorption of monodentate carbonate (weak basic site) and polydentate carbonate (strong basic site), respectively (Ewald and Hinrichsen, 2019; Grünbacher et al., 2019; Zheng et al., 2019), appeared in L-Ni/γ-Al_2O_3. The intensity of these two peaks intensified with Ni loading and a new desorption peak at 500°C appeared, which was possibly derived from a kind of bidentate carbonate (Busca and Lorenzelli, 1982). More bidentate carbonate desorbed at around 430°C (moderate basic site) over H-Ni/γ-Al_2O_3 (Ewald and Hinrichsen, 2019). Carbonates were generally thought to be formed through two ways: CO_2 might combine with the pre-adsorbed oxygen on the metal surface to form carbonate or it could directly form carbonate on the support near the metal-support interface (Bitter et al., 1998; Solymosi, 1991). Combined with the results above, it was possible that on the bounded Ni with stronger MSI, the O atom of the support might participate in the formation of polydentate carbonate. The CO signal (m/z = 28) in CO_2-TPD MS of the fresh catalysts is also given in Figure S22 to imply the capability for CO_2 activation. H-Ni/γ-Al_2O_3 showed a distinct peak at 425°C, while M-Ni/γ-Al_2O_3 exhibited a lower temperature peak at 340°C beside the peak at 425°C. This suggested that M-Ni/γ-Al_2O_3 had better CO_2 activation ability to produce CO and active O* than H-Ni/γ-Al_2O_3, and it could be inferred that CO_2 was easier to be activated on the bounded Ni than the free state Ni.

Furthermore, CO_2-TPSR DRIFTS at different temperature was explored to assess CO_2 activation ability and CO adsorption ability at the same time, and relevant results are shown in Figure S23. It was easy to find that CO species at ~2100 cm^{-1} began to appear at 400–450°C for H-Ni/γ-Al_2O_3 (Tang et al., 2017), which was in good agreement with the results of CO_2-TPD MS, and CO peaks intensity increased monotonically with the temperature. However, almost no peak of CO was found in M-Ni/γ-Al_2O_3. This could be weaker CO adsorption ability of the bounded Ni in M-Ni/γ-Al_2O_3, thanks to rational MSI compared with the free state Ni in H-Ni/γ-Al_2O_3. As reported in relevant articles, strong MSI would weaken the adsorption strength of small molecules such as CO and H_2 on metal particles (Han et al., 2020), and the free energy of C-C coupling would increase significantly due to enhanced MSI (Zhang et al., 2021b). Hence, the CO disproportionation reaction (Boudouard reaction) would be inhibited due to these above reasons on the bounded Ni, thereby reducing the accumulation of carbon depositions.

In situ DRIFTS was performed to explore the differences of the DRM reaction mechanism between the bounded Ni and the free state Ni, and the results are given in Figures 4C and 4D. As shown in Figure 4C for M-Ni/γ-Al_2O_3, the peaks of polydentate carbonate (a broad peak around 1400–1500 cm^{-1}), bidentate carbonate (1558 cm^{-1}), and bidentate formate (1542 cm^{-1}) were found during the reaction, which meant that these species were the reactive intermediates (Binet et al., 1999; Takano et al., 2016). Different from the results of the M-Ni/γ-Al_2O_3, the peak of polydentate carbonate species was not shown over H-Ni/γ-Al_2O_3 (Figure 4D). Instead, peaks assigned to monodentate carbonate at 1506 cm^{-1} appeared during the reaction (Binet *et al.*, 1999), which was not observed in M-Ni/γ-Al_2O_3. At the same time, the peaks of bidentate formate at 1542 cm^{-1} and bidentate carbonate at 1558 cm^{-1} were also observed. However, it was interesting to find that the peak intensity of monodentate carbonate and bidentate carbonate strengthened and weakened alternately. This phenomenon showed that the monodentate and bidentate carbonates would transform into each other during the reaction. According to previous literature, monodentate carbonates did tend to be converted into bidentate carbonates (Galenda et al., 2010). Combined with the conclusions of the catalysts' TOF value, it could be proposed that the interconversion would delay the conversion from carbonate to formate, thus hindering the conversion of CO_2.

Reaction mechanism studies

The mechanism schematic is given in Figure 5 summarized from the previous analysis. For M-Ni/γ-Al_2O_3 sample, where only the bounded Ni existed, CH_4 was activated more effectively to produce CH_x and H_2. The activation of CO_2 on M-Ni/γ-Al_2O_3 was divided into two ways: on the one hand, CO_2 could directly decompose into active O* and CO, the active O* then reacted with CH_x species (x = 0, 1, 2, 3) to generate CH_xO, and finally CH_xO would degrade directly or indirectly to produce H_2 and CO (Zhu et al., 2009). On the

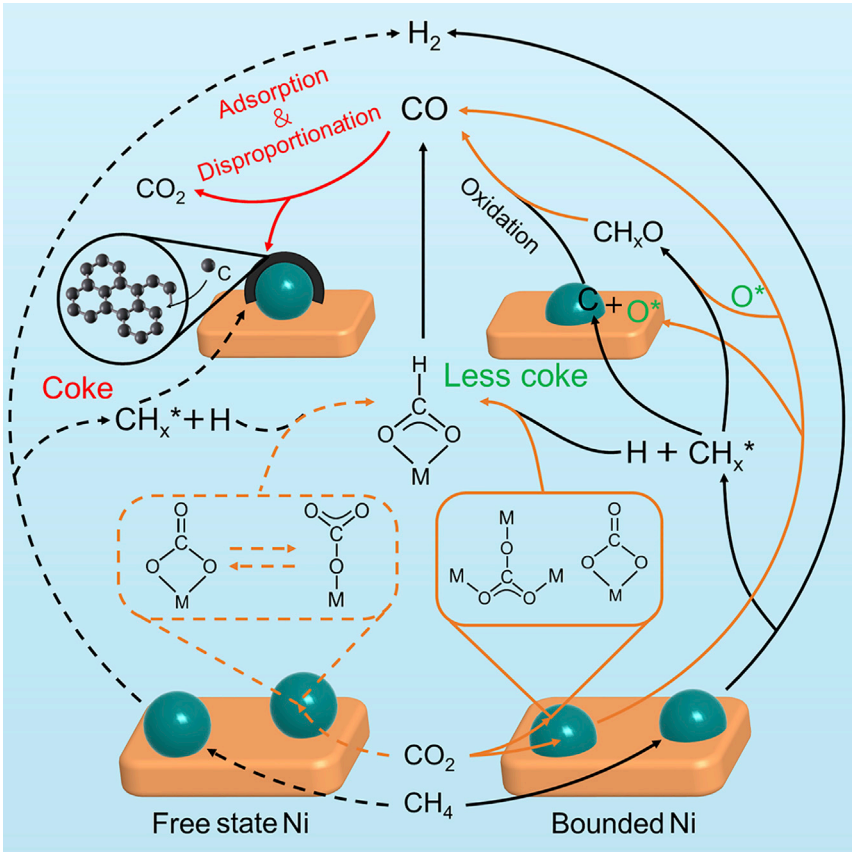

Figure 5. Proposed DRM mechanism diagram on the bounded Ni and the free state Ni

other hand, CO_2 was mainly adsorbed and activated on the catalysts in form of the polydentate/bidentate carbonate, as observed in CO_2-TPD. It could be inferred that the three ligands of the polydentate carbonate might involve Al and Ni atoms simultaneously considering the strong interaction between Ni and γ-Al_2O_3 at the metal-support interface. And the polydentate carbonate was believed to guarantee both the high activity and good coke resistance of the catalysts for DRM by forming Ni-Al surface as reported in a recent literature (Chen et al., 2020). The polydentate/bidentate carbonate could later quickly react with H* species to form bidentate formate, which would subsequently decompose into CO and H_2. This efficient conversion would further accelerate CH_4 decomposition on the bounded Ni, proved by the results of CH_4-CO_2-TPSR-MS. The desorption of the product (H_2 and CO) and C-O coupling on the bounded Ni was preferred due to rational MSI (Han *et al.*, 2020; Zhang et al., 2021b), so the side reactions (Reverse water gas shift (RWGS) and Boudouard reaction) were suppressed, thus reducing the coke deposition. As for the H-Ni/γ-Al_2O_3, where the bounded Ni and the free state Ni coexisted, CO_2 might preferentially adsorb and be activated in the form of the bidentate and monodentate carbonate. The bidentate formate was then formed via a reaction between H* and the carbonate intermediates (Bobadilla et al., 2017). However, this process was blocked to a certain extent since interconversion between the carbonates at the same time. This finding could explain why the TOF of CO_2 of M-Ni/γ-Al_2O_3 was higher than that of the H-Ni/γ-Al_2O_3. Furthermore, the free state Ni with weaker MSI got stronger CO adsorption ability than that of the bounded Ni. The stronger CO adsorption ability meant more CO accumulation on the surface of catalysts during the reaction, which would exacerbate CO disproportionation and thus causing more serious coking. In summary, a rational MSI with γ-Al_2O_3 made the bounded Ni more capable of activating CO_2, which in turn promoted the conversion of CH_4 and the elimination of carbon depositions, and also facilitated the desorption of CO, thereby addressing the trade-off issue of catalytic activity and carbon resistance.

DISCUSSION

In this study, we made an insight into the differences between the bounded Ni and the free state Ni in Ni/γ-Al_2O_3 for DRM reaction in terms of carbon resistance and reaction mechanism. The bounded nickel, which held rational MSI, showed better coking resistance, higher TOF_{CO2} and TOF_{CH4} than the free state nickel due to the better CH_4 cracking ability, and CO_2 adsorption and activation. CO_2 adsorbed on the bounded Ni mainly in the form of the polydentate/bidentate carbonate and converted into bidentate formate efficiently, which finally decomposed into CO. By contrast, the interconversion between monodentate carbonate and bidentate carbonate was detected on the free state Ni, which would slow down the conversion efficiency of CO_2 and further reduced the TOF of CH_4. Moreover, the CO generated by the reaction was easier to desorb from the bounded Ni compared with the free state Ni due to rational MSI, which would further improve coking resistance by inhibiting the CO disproportionation. We believed that our observations would strengthen the understanding of structure-performance relationship in catalysis and could enable the design of more efficient catalysts for DRM in the future.

Limitations of the study

In this study, we explored the differences in the DRM performance and reaction mechanism of two different active Ni species (the bounded Ni and the free state Ni) over Ni/γ-Al_2O_3, which would be useful for the future design of high-performance DRM catalysts. However, the work also has some shortcomings. For example, it might be difficult to control the size of the Ni particles obtained by the exsolution to reach the cluster level according to relevant researches, so studying the DRM properties of smaller Ni species (such as Ni_1, Ni_2, and Ni_4) would be more interesting, although it also seems more difficult but is worth exploring.

SUPPLEMENTAL INFORMATION

Supplemental information can be found online at https://doi.org/10.1016/j.isci.2021.102747.

STAR★METHODS

Detailed methods are provided in the online version of this paper and include the following:

- KEY RESOURCES TABLE
- RESOURCE AVAILABILITY
  - Lead contact
  - Materials availability
  - Data and code availability
- METHOD DETAILS
  - Catalyst preparation
  - Instrumentation and characterization
  - Thermo-catalytic test

ACKNOWLEDGMENTS

B.Y. and J.D. contributed equally to this work. We thank for the financial support from the National Key R&D Program of China (2017YFE0132400). We also appreciate the support for catalyst characterization from the Analysis and Testing Center of Shanghai University.

AUTHOR CONTRIBUTIONS

Conceptualization, B.Y. and D.Z.; investigation, B.Y. and D.Z.; validation, B.Y. and J.D.; formal analysis, B.Y., J.D., and H.L.; writing – original draft, B.Y. and J.D.; writing – review & editing, B.Y., J.D., and D.Z.; data curation, T.Y. and H.L.; resources, D.Z. and J.Z.; funding acquisition, D.Z.; supervision, D.Z.

DECLARATION OF INTERESTS

The authors declare no competing interests.

Received: April 15, 2021
Revised: May 25, 2021
Accepted: June 14, 2021
Published: July 23, 2021

SUPPORTING CITATIONS

The following references appear in the Supplemental information: Akri et al., 2019; Kim et al., 2017; Li et al., 2017; Wang et al., 2018; Zhu et al., 2008.

REFERENCES

Akri, M., Zhao, S., Li, X., Zang, K., Lee, A.F., Isaacs, M.A., Xi, W., Gangarajula, Y., Luo, J., Ren, Y., et al. (2019). Atomically dispersed nickel as coke-resistant active sites for methane dry reforming. Nat. Commun. *10*, 5181.

Al-Fatesh, A.S., Kumar, R., Kasim, S.O., Ibrahim, A.A., Fakeeha, A.H., Abasaeed, A.E., Alrasheed, R., Bagabas, A., Chaudhary, M.L., Frusteri, F., and Chowdhury, B. (2020). The effect of modifier identity on the performance of Ni-based catalyst supported on γ-Al_2O_3 in dry reforming of methane. Catal. Today *348*, 236–242.

Binet, C., Daturi, M., and Lavalley, J.C. (1999). IR study of polycrystalline ceria properties in oxidised and reduced states. Catal. Today *50*, 207–225.

Bitter, J.H., Seshan, K., and Lercher, J.A. (1998). Mono and bifunctional pathways of CO_2/CH_4 reforming over Pt and Rh based catalysts. J. Catal. *176*, 93–101.

Bobadilla, L.F., Garcilaso, V., Centeno, M.A., and Odriozola, J.A. (2017). Monitoring the reaction mechanism in model biogas reforming by in situ transient and steady-state DRIFTS measurements. ChemSusChem *10*, 1193–1201.

Bu, K., Deng, J., Zhang, X., Kuboon, S., Yan, T., Li, H., Shi, L., and Zhang, D. (2020). Promotional effects of B-terminated defective edges of Ni/boron nitride catalysts for coking-and sintering-resistant dry reforming of methane. Appl. Catal., B *267*, 118692.

Bu, K., Kuboon, S., Deng, J., Li, H., Yan, T., Chen, G., Shi, L., and Zhang, D. (2019). Methane dry reforming over boron nitride interface-confined and LDHs-derived Ni catalysts. Appl. Catal., B *252*, 86–97.

Busca, G., and Lorenzelli, V.L. (1982). Infrared spectroscopic identification of species arising from reactive adsorption of carbon oxides on metal oxide surfaces. Mater. Chem. *7*, 89–126.

Cao, Y., Maitarad, P., Gao, M., Taketsugu, T., Li, H., Yan, T., Shi, L., and Zhang, D. (2018). Defect-induced efficient dry reforming of methane over two-dimensional Ni/h-boron nitride nanosheet catalysts. Appl. Catal. B *238*, 51–60.

Chen, S., Zaffran, J., and Yang, B. (2020). Descriptor design in the computational screening of Ni-based catalysts with balanced activity and stability for dry reforming of methane reaction. ACS Catal. *10*, 3074–3083.

Dama, S., Ghodke, S.R., Bobade, R., Gurav, H.R., and Chilukuri, S. (2018). Active and durable alkaline earth metal substituted perovskite catalysts for dry reforming of methane. Appl. Catal. B *224*, 146–158.

Das, S., Ashok, J., Bian, Z., Dewangan, N., Wai, M., Du, Y., Borgna, A., Hidajat, K., and Kawi, S. (2018). Silica-ceria sandwiched Ni core-shell catalyst for low temperature dry reforming of biogas: coke resistance and mechanistic insights. Appl. Catal. B *230*, 220–236.

Dong, J., Fu, Q., Li, H., Xiao, J., Yang, B., Zhang, B., Bai, Y., Song, T., Zhang, R., Gao, L., et al. (2020). Reaction-induced strong metal-support interactions between metals and inert boron nitride nanosheets. J. Am. Chem. Soc. *142*, 17167–17174.

Elias, I., Soon, A., Huang, J., Haynes, B.S., and Montoya, A. (2019). Atomic order, electronic structure and thermodynamic stability of nickel aluminate. Phys. Chem. Chem. Phys. *21*, 25952–25961.

Ewald, S., and Hinrichsen, O. (2019). On the interaction of CO_2 with Ni-Al catalysts. Appl. Catal. A. *580*, 71–80.

Fletcher, S.E.M., and Schaefer, H. (2019). Rising methane: a new climate challenge. Science *364*, 932–933.

Foppa, L., Margossian, T., Kim, S.M., Müller, C., Copéret, C., Larmier, K., and Comas-Vives, A. (2017). Contrasting the role of Ni/Al_2O_3 interfaces in water-gas shift and dry reforming of methane. J. Am. Chem. Soc. *139*, 17128–17139.

Foppa, L., Silaghi, M.C., Larmier, K., and Comas Vives, A. (2016). Intrinsic reactivity of Ni, Pd and Pt surfaces in dry reforming and competitive reactions: insights from first principles calculations and microkinetic modeling simulations. J. Catal. *343*, 196–207.

Galenda, A., Natile, M.M., Nodari, L., and Glisenti, A. (2010). $La_{0.8}Sr_{0.2}Ga_{0.8}Fe_{0.2}O_{3-\delta}$: influence of the preparation procedure on reactivity toward methanol and ethanol. Appl. Catal. B *97*, 307–322.

Grünbacher, M., Klötzer, B., and Penner, S. (2019). CO_2 reduction by hydrogen pre-reduced acceptor-doped ceria. ChemPhysChem *20*, 1706–1718.

Han, B., Guo, Y., Huang, Y., Xi, W., Xu, J., Luo, J., Qi, H., Ren, Y., Liu, X., Qiao, B., and Zhang, T. (2020). Strong metal-support interactions between Pt single atoms and TiO_2. Angew. Chem. Int. Ed. *59*, 11824–11829.

Joo, S., Seong, A., Kwon, O., Kim, K., Lee, J.H., Gorte, R.J., Vohs, J.M., Han, J.W., and Kim, G. (2020). Highly active dry methane reforming catalysts with boosted in situ grown Ni-Fe nanoparticles on perovskite via atomic layer deposition. Sci. Adv. *6*, eabb1573.

Keturakis, C.J., Ni, F., Spicer, M., Beaver, M.G., Caram, H.S., and Wachs, I.E. (2014). Monitoring solid oxide CO_2 capture sorbents in action. ChemSusChem *7*, 3459–3466.

Kim, S.M., Abdala, P.M., Margossian, T., Hosseini, D., Foppa, L., Armutlulu, A., van Beek, W., Comas Vives, A., Copéret, C., and Müller, C. (2017). Cooperativity and dynamics increase the performance of NiFe dry reforming catalysts. J. Am. Chem. Soc. *139*, 1937–1949.

Li, S., and Gong, J. (2014). Strategies for improving the performance and stability of Ni-based catalysts for reforming reactions. Chem. Soc. Rev. *43*, 7245–7256.

Li, X., Li, D., Tian, H., Zeng, L., Zhao, Z., and Gong, J. (2017). Dry reforming of methane over Ni/La_2O_3 nanorod catalysts with stabilized Ni nanoparticles. Appl. Catal., B *202*, 683–694.

Li, Z., Mo, L., Kathiraser, Y., and Kawi, S. (2014). Yolk-satellite-shell structured Ni-yolk@Ni@SiO_2 nanocomposite: superb catalyst toward methane CO_2 reforming reaction. ACS Catal. *4*, 1526–1536.

Margossian, T., Larmier, K., Kim, S.M., Krumeich, F., Fedorov, A., Chen, P., Müller, C.R., and Copéret, C. (2017). Molecularly tailored nickel precursor and support yield a stable methane dry reforming catalyst with superior metal utilization. J. Am. Chem. Soc. *139*, 6919–6927.

Mette, K., Kühl, S., Tarasov, A., Willinger, M.G., Kröhnert, J., Wrabetz, S., Trunschke, A., Scherzer, M., Girgsdies, F., and Düdder, H. (2016). High-temperature stable Ni nanoparticles for the dry reforming of methane. ACS Catal. *6*, 7238–7248.

Négrier, F., Marceau, E., Che, M., Giraudon, J.M., Gengembre, L., and Lōfberg, A. (2005). A systematic study of the interactions between chemical partners (metal, ligands, counterions, and support) involved in the design of Al_2O_3-supported nickel catalysts from diamine-Ni(II) chelates. J. Phys. Chem. B *109*, 2836–2845.

Osaki, T., Masuda, H., Horiuchi, T., and Mori, T. (1995). Highly hydrogen-deficient hydrocarbon species for the CO_2-reforming of CH_4 on Co/Al_2O_3 catalyst. Catal. Lett. *34*, 59–63.

Pakhare, D., and Spivey, J. (2014). A review of dry (CO_2) reforming of methane over noble metal catalysts. Chem. Soc. Rev. *43*, 7813–7837.

Rahman, M.A., Radhakrishnan, R., and Gopalakrishnan, R. (2018). Structural, optical, magnetic and antibacterial properties of Nd doped NiO nanoparticles prepared by co-precipitation method. J. Alloys Compd. *742*, 421–429.

Rogers, J.L., Mangarella, M.C., D'Amico, A.D., Gallagher, J.R., Dutzer, M.R., Stavitski, E., Miller, J.T., and Sievers, C. (2016). Differences in the nature of active sites for methane dry reforming and methane steam reforming over nickel aluminate catalysts. ACS Catal. *6*, 5873–5886.

Shehu, H., Gobina, E., and Orakwe, I. (2019). Utilization of CO_2 for syngas production by CH_4 partial oxidation using a catalytic membrane reactor. Int. J. Hydrogen Energy *44*, 9896–9905.

Shi, L., Yang, G., Tao, K., Yoneyama, Y., Tan, Y., and Tsubaki, N. (2013). An introduction of CO_2 conversion by dry reforming with methane and

new route of low-temperature methanol synthesis. Acc. Chem. Res. *46*, 1838–1847.

Solymosi, F. (1991). The bonding, structure and reactions of CO_2 adsorbed on clean and promoted metal surfaces. J. Mol. Catal. *65*, 337–358.

Song, K., Lu, M., Xu, S., Chen, C., Zhan, Y., Li, D., Au, C., Jiang, L., and Tomishige, K. (2018). Effect of alloy composition on catalytic performance and coke-resistance property of Ni-Cu/Mg(Al)O catalysts for dry reforming of methane. Appl. Catal. B *239*, 324–333.

Song, Y., Ozdemir, E., Ramesh, S., Adishev, A., Subramanian, S., Harale, A., Albuali, M., Fadhel, B.A., Jamal, A., Moon, D., et al. (2020). Dry reforming of methane by stable Ni-Mo nanocatalysts on single-crystalline MgO. Science *367*, 777.

Srifa, A., Kaewmeesri, R., Fang, C., Itthibenchapong, V., and Faungnawakij, K. (2018). $NiAl_2O_4$ spinel-type catalysts for deoxygenation of palm oil to green diesel. Chem. Eng. J. *345*, 107–113.

Stroud, T., Smith, T.J., Le Saché, E., Santos, J.L., Centeno, M.A., Arellano Garcia, H., Odriozola, J.A., and Reina, T.R. (2018). Chemical CO_2 recycling via dry and bi reforming of methane using Ni-Sn/Al_2O_3 and Ni-Sn/CeO_2-Al_2O_3 catalysts. Appl. Catal. B *224*, 125–135.

Takano, H., Kirihata, Y., Izumiya, K., Kumagai, N., Habazaki, H., and Hashimoto, K. (2016). Highly active Ni/Y-doped ZrO_2 catalysts for CO_2 methanation. Appl. Surf. Sci. *388*, 653–663.

Tang, H., Su, Y., Zhang, B., Lee, A.F., Isaacs, M.A., Wilson, K., Li, L., Ren, Y., Huang, J., Haruta, M., et al. (2017). Classical strong metal-support interactions between gold nanoparticles and titanium dioxide. Sci. Adv. *3*, e1700231.

Wang, N., Shen, K., Huang, L., Yu, X., Qian, W., and Chu, W. (2013). Facile route for synthesizing ordered mesoporous Ni-Ce-Al oxide materials and their catalytic performance for methane dry reforming to hydrogen and syngas. ACS Catal. *3*, 1638–1651.

Wang, Y., Yao, L., Wang, Y., Wang, S., Zhao, Q., Mao, D., and Hu, C. (2018). Low-temperature catalytic CO_2 dry reforming of methane on Ni-Si/ZrO_2 catalyst. ACS Catal. *8*, 6495–6506.

Wong, Y.J., Koh, M.K., Khairudin, N.F., Ichikawa, S., Morikawa, Y., and Mohamed, A.R. (2019). Development of Co supported on Co-Al spinel catalysts from exsolution of amorphous Co-Al oxides for carbon dioxide reforming of methane. ChemCatChem *11*, 5593–5605.

Xu, Z., Li, Y., Zhang, J., Chang, L., Zhou, R., and Duan, Z. (2001). Bound-state Ni species —— a superior form in Ni-based catalyst for CH_4/CO_2 reforming. Appl. Catal. A. *210*, 45–53.

Zhang, L., Wang, X., Shang, X., Tan, M., Ding, W., and Lu, X. (2017). Carbon dioxide reforming of methane over mesoporous nickel aluminate/γ-alumina composites. J. Energy Chem. *26*, 93–100.

Zhang, S., Muratsugu, S., Ishiguro, N., and Tada, M. (2013). Ceria-doped Ni/SBA-16 catalysts for dry reforming of methane. ACS Catal. *3*, 1855–1864.

Zhang, F., Li, Y.H., Qi, M.Y., Yamada, Y.M.A., Anpo, M., Tang, Z.R., and Xu, Y.J. (2021a). Photothermal catalytic CO_2 reduction over nanomaterials. Chem. Catal. *1*, 1–26.

Zhang, Y., Yao, Y.F., Qiao, Y.Y., and Wang, G.C. (2021b). First-principles theoretical study on dry reforming of methane over perfect and boron-vacancy-containing h-BN sheet-supported Ni catalysts. Phys. Chem. Chem. Phys. *23*, 617–627.

Zhao, Y., Kang, Y., Li, H., and Li, H. (2018). CO_2 conversion to synthesis gas via DRM on the durable Al_2O_3/Ni/Al_2O_3 sandwich catalyst with high activity and stability. Green. Chem. *20*, 2781–2787.

Zheng, X., Li, Y., Zhang, L., Shen, L., Xiao, Y., Zhang, Y., Au, C., and Jiang, L. (2019). Insight into the effect of morphology on catalytic performance of porous CeO_2 nanocrystals for H_2S selective oxidation. Appl. Catal. B *252*, 98–110.

Zhou, L., Li, L., Wei, N., Li, J., and Basset, J.M. (2015). Effect of $NiAl_2O_4$ formation on Ni/Al_2O_3 stability during dry reforming of methane. ChemCatChem *7*, 2508–2516.

Zhu, Y.A., Chen, D., Zhou, X.G., and Yuan, W.K. (2009). DFT studies of dry reforming of methane on Ni catalyst. Catal. Today *148*, 260–267.

Zhu, X., Huo, P., Zhang, Y., Cheng, D., and Liu, C. (2008). Structure and reactivity of plasma treated Ni/Al_2O_3 catalyst for CO_2 reforming of methane. Appl. Catal., B *81*, 132–140.

STAR★METHODS

KEY RESOURCES TABLE

REAGENT or RESOURCE	SOURCE	IDENTIFIER
Chemicals, peptides, and recombinant proteins		
γ-Al_2O_3	Titan Scientific Co., Ltd	CAS: 1344-28-1
Nickel(II) nitrate hexahydrate $Ni(NO_3)_2{\cdot}6H_2O$	Sinopharm Chemical Reagent Co., Ltd.	CAS: 13478-00-7

RESOURCE AVAILABILITY

Lead contact

Further information and requests for resources and reagents should be directed to and will be fulfilled by the lead contact, Dengsong Zhang (dszhang@shu.edu.cn)

Materials availability

This study did not generate new unique reagents. All chemicals were obtained from commercial resources and used as received.

Data and code availability

This study did not generate any datasets or code. All relevant data are available from the corresponding author (dszhang@shu.edu.cn) upon reasonable request.

METHOD DETAILS

Catalyst preparation

Catalysts in this work were prepared by simple impregnation methods. The experimental steps were as follows: For the preparation of 0.9 wt%/1.5 wt%/5.0 wt% Ni/γ-Al_2O_3, 0.045 g/0.075 g/0.261 g $Ni(NO_3)_2{\cdot}6H_2O$, 30 mL H_2O and 1 g γ-Al_2O_3 was mixed and stirred for 6 h, then the sample was stored in an 80 °C oven overnight after rotary evaporation. The dried sample was fully ground and calcined in a muffle furnace (calcined at 650 °C for 3 h, heating rate 10 °C/min) to obtain the calcined samples. Finally, the calcined sample underwent reduction treatment to obtain a fresh reduced sample (reduction conditions: reduction at 750 °C for 1 h, 10% H_2/N_2, heating rate 10 °C/min).

Instrumentation and characterization

High-resolution Transmission Electron Microscopy and Transmission Electron Microscopy (HRTEM and TEM) images were gathered on JEM-2010F and JEM-2100F. X-Ray Diffraction (XRD) was performed using a Bruker D8 Advance diffractometer equipped with a Cu Ka radiation source and the scanning range was 10-90°, then the size of Ni NPs was calculated via the Scherrer equation. Thermo Gravimetric Analysis (TGA) was measured on NETZSCH STA 449 F1 with the temperature range from 50 to 800 °C (ramping rate: 10 °C/min) in the air to analyze the weight of coke on the spent catalysts. The specific surface area was tested on Autosorb-iQ2 by nitrogen absorption and desorption methods, and then calculated by the Brunauer-Emmett-Teller formula. The ability of the catalyst to adsorb and activate CO_2 was measured using CO_2-TPD MS. Typically, 0.080 g fresh samples were pretreated at 300 °C for 0.5 h under He atmosphere, then introducing 10% CO_2/He for 60 min with a gas flow of 30 mL min^{-1}, after removing weakly-absorbed CO_2 using He (30 mL·min^{-1}), the device was gradually heated from 50 °C to 800 °C, and the exhaust gas was passed to the mass spectrometry for analysis.

CO-TPD MS was used to detect the CO adsorption ability of the catalysts. The sample was firstly pretreated for 30 min at 300°C in a He atmosphere (30 mL/min). After the temperature was cooled to room temperature, 99% CO was passed for 30 minutes. Then switching to He purge again for 30 min to remove the weakly-adsorbed CO molecules. Finally, the temperature was raised to 800 °C at 10 °C/min and the GC and MS signals were recorded.

TPR-TPO tests were implemented on a Micromeritics AutoChem II 2920 device. 0.08 g calcination sample was firstly pre-treated for 0.5 h at 300 °C under He (30 mL min^{-1}), then it was heated from 50 to 750 °C and reduced at 750 °C for 60 min. When the equipment was cooled to 50 °C, the TPO step was started: after the same pretreatment, 2% O_2/He (30 mL min^{-1}) was introduced, and the temperature was gradually heated to 900°C while the results were analyzed with a TCD detector. The Micromeritics AutoChem II 2950 was used to detect Ni dispersion using H_2 pulse titration. The calcination sample was firstly in-situ reduced using 10% H_2/Ar for 60 min at 750 °C, after cooling down to the set temperature, the H_2 pulse titration was started to operate until the adsorption capacity was saturated. UV-vis spectra of the catalysts were collected on Agilent Technologies Cary Series, using $BaSO_4$ or γ-Al_2O_3 as the baseline.

TPSR tests coupled with MS were tested on Micromeritics AutoChem II 2920 combined with Thermostar™ Pfeiffer. For CH_4-TPSR, fresh-reduced samples were present in the equipment, then the pretreatment was performed under helium with 30 mL/min while the device was heated to 300 °C (10 °C/min) to purge away physically adsorbed impurities. After cooling down to 50 °C and the baseline was stable, CH_4 flow was introduced continuously and the quartz tube would be heated to 800 °C, the product gas mixture was analyzed in Thermostar™ Pfeiffer. In CO_2-CH_4-TPSR tests, the same pretreatment was done followed by CO_2 pre-adsorption process at 50 °C, and CH_4 was injected to accomplish surface reaction on the fresh samples. Individual CO_2-TPSR was not done here because CO_2 activation of the catalysts was so weak that the outcome gas could not be well differentiated.

Operando Raman spectra were recorded on the LabRAM HR Evolution. A Spectra range of 1000−2000 cm^{-1} was used to observe changes of carbon species during the reaction in real-time, and a laser with a wavelength of 532 nm was adopted. The spectral resolution was 4 cm^{-1}, spectra over serial Ni/γ-Al_2O_3 catalysts were collected at 650 °C for 120 min, with reaction gas flow (CH_4/CO_2 = 15/15 mL/min), N_2 (30 mL/min) was individually introduced when the device was heated and spectra were recorded. *In situ* DRIFTS was operated on Nicolet is50 FT-IR spectrometer. For all DIFTTS tests, fresh catalysts were pre-treated at 300 °C under the N_2 (30 mL/min), and the background spectrum at different temperatures was collected after the pretreatment, at last, the experimental spectrum was collected according to the specific experimental situation. For CO_2 adsorption DRIFTS, CO_2 (10 mL/min) was pre-adsorbed on the catalyst for 30 min, then raising the temperature and pick a point every 50 °C, from 100 °C-700 °C. Temperature-programmed reactions were firstly tested from 300 °C to 700 °C in a gas mixture of CH_4:CO_2:N_2 =10: 10: 30 mL·min^{-1}, then reaction 650 °C was chosen to explore the differences in the changes of reaction intermediates during the reaction of different samples, with the same gas flow rate and spectral information at different points in time were collected.

Thermo-catalytic test

For the DRM test section, the fresh catalysts (0.12 g) were placed directly in the quartz tube (inner diameter 8 mm), without any dilution or compression. Then passing the pure reaction gas mixture (CH_4 : CO_2 = 25:25 mL/min) into the reaction tube to take the baseline, and the off-gas was analyzed by gas chromatography equipped with a thermal conductivity detector (TCD). After the baseline was stable, the reaction gas inlet volume was determined by reading the TCD peak area. Then switching to 30 mL/min of N_2, raising the temperature to the reaction temperature at a rate of 10 °C/min, and then switching back to the pure reaction gas for DRM test for 20 h. After the tail gas was analyzed by TCD, the peak area of the corresponding species was obtained. For the TOF test, 0.007/0.015/0.02 g catalysts were used in the TOF test for H, M, L-Ni/γ-Al_2O_3, respectively (Gas flow rate for CH_4 and CO_2: 50 mL/min). The conversion rate of the reactant could be calculated from the baseline peak area and the peak area during the reaction. The H_2/CO ratio of the product could be obtained from the TCD peak area and the correction factor (the correction factor was measured in advance through the external standard method through the standard gas). The calculation formulas were as follows:

The conversion rate of the reactant was calculated like following:

$$X_{CH_4}(\%) = 100 * \frac{CH_4]_{baseline} - CH_4]_{reaction}}{CH_4]_{baseline}}$$

$$X_{CO_2}(\%) = 100 * \frac{CO_2]_{baseline} - CO_2]_{reaction}}{CO_2]_{baseline}}$$

The H_2/CO ratio was calculated by:

$$\frac{H_2}{CO} = \frac{H_2 \text{ produced}}{CO \text{ produced}} * \left(\frac{H_2}{CO}\right)_{calibration}$$

The apparent reaction rates (u) were calculated by the following equation.

$$u = (V \text{ mL/min} \div 22.4 \text{ L/mol} \times \alpha)/(m \times w)$$

TOF values were calculated by the following equation.

$$TOF = (V \text{ mL/min} \div 22.4 \text{ L/mol}) \times \alpha)/(2 \times m \times n)$$

V represents the volume flow rate of the corresponding reactant (CH_4 or CO_2), 22.4 was the molar volume of the standard gas, α was reactant conversion under kinetic control, m was catalysts mass used in the test, w represented the Ni loading measured by ICP (Inductively Coupled Plasma) results given in Table S5, n represented H_2 consumption in the H_2-pulse tests (Table S6 for more details), 2 meant that two Ni atoms were used to adsorb one H_2 molecule.

The weight hourly space velocity (WHSV) of the reaction was calculated as follows:

$$WHSV = \frac{(25+25)\frac{mL}{min} \times 60\frac{min}{h}}{0.12 \text{ g}_{cat}} = 25000 \text{ mL} \cdot h^{-1} \cdot g_{cat}^{-1}$$